# A JWST Preview: Adaptive-optics Images of H₂, Br-γ, and K-continuum in Carina's Western Wall

Patrick Hartigan[1] , Turlough Downes[2] , and Andrea Isella[1] 
[1] Physics and Astronomy Department, Rice University, 6100 S. Main, Houston, TX 77005-1892, USA; hartigan@sparky.rice.edu
[2] Centre for Astrophysics & Relativity, School of Mathematical Sciences, Dublin City University, Glasnevin, Dublin 9, Ireland

## Abstract

We present the first wide-field near-infrared adaptive-optics images of Carina's Western Wall (G287.38-0.62), one of the brightest and most well-defined irradiated interfaces known in a region of massive star formation. The new narrowband H₂ 2.12 $\mu$m, Br-γ and K-continuum images from Gemini South trace the photoevaporative flow from the cloud and identify locations where UV radiation from the surrounding massive stars excites molecular hydrogen to fluoresce. With a field of view of $\sim$1′.5 $\times$ 2′.9 and spatial resolution between 60 and 110 mas, the new images show a spectacular level of detail over a large area, and presage what the James Webb Space Telescope (JWST) should achieve. The Wall is convex in shape, with a large triangular-shaped extension near its apex. The interface near the apex consists of 3–4 regularly spaced ridges with projected spacings of $\sim$2000 au, suggestive of a large-scale dynamically important magnetic field. The northern edge of the Wall breaks into several swept-back fragments of width $\sim$1800 au that resemble Kelvin–Helmholtz instabilities, and the southern part of the Wall also shows complex morphologies including a sinusoidal-like variation with a half-wavelength of 2500 au. Though the dissociation front must increase the density along the surface of the Wall, it does not resolve into pillars that point back to the ionization sources, as could occur if the front triggered new stars to form. We discovered that MHO 1630, an H₂ outflow with no clear driving source in the northern portion of the Wall, consists of a series of bow shocks arrayed in a line.

## 1. Introduction

Star formation occurs both within low-mass dark clouds and inside large molecular cloud complexes, but the role radiation plays in the two types of regions differs markedly (e.g., Tan et al. 2014 for a review). Unlike their more quiescent counterparts, giant molecular clouds typically form O and B stars, and ultraviolet radiation from these massive stars injects enough energy into the surrounding medium to create large H II regions. The resulting volumes of expanding ionized gas remove material that might otherwise accrete onto a protostar, while radiation photoevaporates the outer portions of disks and may alter the spectrum of stellar masses created in the region (Krumholz et al. 2011; Winter et al. 2018). On the other hand, density waves driven into molecular clouds by radiation from massive stars could also potentially trigger new stars to form, either directly as the fronts compress existing clumps into gravitationally unstable cores, or indirectly if the fronts increase the overall density in a cloud to the point where subsequent collisions between cloud fragments induce collapse (e.g., Haworth & Harries 2011). Radiative feedback and winds from newly formed stars into the nascent cloud material also drive structures on scales of tens or even hundreds of parsecs, and create sequential episodes of star formation (e.g., Venuti et al. 2018) and clear out chimneys and bubbles perpendicular to the galactic plane (Robitaille et al. 2018). On smaller scales, how massive stars form remains a topic of intense theoretical work, as models must include the effects of strong radiation pressure and photoevaporation from massive protostars that both limit the available timescale for accretion and may widen existing outflow cavities (Rosen et al. 2016; Tanaka et al. 2017).

To understand quantitatively how intense radiation fields from young massive stars affect star formation in molecular clouds, we must assess parsec scales, where filaments respond to the influence of large-scale magnetic fields, smaller scales of order 0.1 pc relevant to core formation and fragmentation, and protostellar disk scales of several hundred au (e.g., Li et al. 2018). The most intense radiation environments occur in regions that produce early O-stars, and even the closest of these are over 1.5 kpc away, so to resolve structures on $\sim$100 au scales requires spatial resolutions better than 0″.1. This increase in resolution of an order of magnitude over typical non-adaptive-optics images holds the key to bridging interstellar scales to Oort cloud scales.

Recent advances in instrumentation, especially with adaptive optics (AO), have made it possible to acquire nearly diffraction-limited images in the near-infrared over a field of view greater than an arcminute in size. Such observations are ideal for tracing large-scale outflows and shock waves in star-forming regions where subarcsecond resolution uncovers morphologies crucial to interpreting the physics at work in these systems (e.g., Bally et al. 2015). Wide-field near-infrared AO images presage what the James Webb Space Telescope (JWST) should deliver when it becomes operational, and complement the highest-resolution Atacama Large Millimeter/submillimeter Array (ALMA) maps of molecular cloud filaments and cores, which also have $\lesssim$1″ resolution (e.g., Cheng et al. 2018).

In this Letter we use the GSAOI AO imager on Gemini to study the Western Wall (G287.38-0.62) in Carina, one of the nearest (2.3 kpc; Lim et al. 2019) and most strongly irradiated
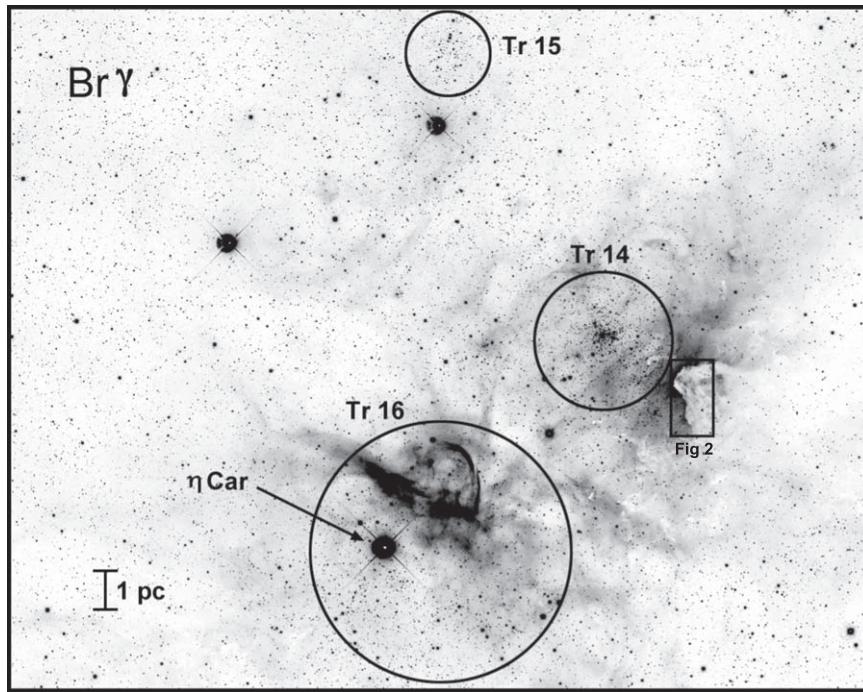
**Figure 1.** Br-$\gamma$ image of the central portion of the Carina star formation region from Hartigan et al. (2015). Locations of the Trumpler 14, 15, and 16 clusters are circled. The boxed area shows the region imaged in Figure 2.

interfaces known to occur in a region of massive star formation. This interface appears as an unassuming dark cloud at optical wavelengths, but it stands out as the brightest feature in the entire Carina complex when imaged in the 2.12 $\mu$m $H_2$ and Br-$\gamma$ emission lines (Hartigan et al. 2015, Figure 1). The $H_2$ 2.12 $\mu$m line is excited by UV fluorescence, and provides a means to trace irradiated interfaces in regions like Carina where UV emission lines are absorbed by dust along the line of sight. The observed spatial offsets between $H_2$ and Br-$\gamma$ emission, the latter arising in a photoevaporative flow as UV radiation ionizes hydrogen, generally agree well with theoretical model predictions (Carlsten & Hartigan 2018). Over a dozen O-stars in the nearby open cluster Tr 14 and a similar number in the cluster Tr 16, including an O2 star (HD 93129A) and an O3.5 star (HD 93129B) in Tr 14 and an O2.5 star (HD 93162) and O3.5 star (ALS 15210) in Tr 16, contribute to the FUV and EUV flux at the Western Wall (Figure 1), as do other O and B stars scattered throughout the region (Gagné et al. 2011; Wu et al. 2018). The Wall has a particularly favorable geometry in that it is a convex structure, which makes it easier to observe interface shapes than in bowl-like concave interfaces like the Orion Bar (Pelligrini et al. 2009; Goicoechea et al. 2016, 2019).

In what follows, we describe our image processing steps and combine the Br-$\gamma$, $H_2$, and K-continuum AO images into a color composite one in Section 2. The images reveal a new $H_2$ outflow and several new features along the interface, including long ridges, sinusoidal-like waves, and fragments that we discuss in Section 3, where we consider what the new observations tell us about instabilities, triggering, and fragmentation processes. A summary of the work is given in Section 4.

## 2. Image Processing

We acquired images of Carina's Western Wall with the Adaptive Optics Imager (GSAOI) on Gemini South between 2018 January 15 and 2018 January 19 for a program with 10 hours of queue time. The images used three narrowband filters, $H_2$ 1–0 S(1) (G1121; $\lambda_o = 2.122$ $\mu$m; $\Delta\lambda = 0.032$ $\mu$m), Br-$\gamma$ (G1122; $\lambda_o = 2.166$ $\mu$m; $\Delta\lambda = 0.032$ $\mu$m), and K-continuum (G1112; $\lambda_o = 2.270$ $\mu$m; $\Delta\lambda = 0.034$ $\mu$m), and employed two pointings offset in decl. from one another by 85″ to cover the region of interest. The center of the composite image is $\alpha = 10$:43:30.6, $\delta = -59$:35:20 (epoch 2000). Within each pointing we used multiple dithers of up to $\pm$ 8″ to remove hot pixels and to fill in the ~3″ gaps between the four Rockwell 2048 × 2048 arrays. Exposure times per dither for the $H_2$, Br-$\gamma$, and K-continuum filters were 120, 120, and 100 s, respectively, with eight nondestructive reads for each exposure. The total exposure times in the northern position were 1320, 1560, and 1400 s, respectively, for $H_2$, Br-$\gamma$, and K-continuum, while the corresponding exposure times for the southern position were 1920, 1680, and 1200 s. We took sets of dithered sky frames without AO correction and with the same exposure times as the object in a relatively blank field located about 20′ away from the object. In all, the data set includes 56 sky frames, enabling us to correct for changing atmospheric backgrounds in each filter as described below.

We combined dome and sky flats with the IRAF packages *gemcombine* and *gemarith*. For each object frame we used the IRAF command *gemexpr* to flat-field the data, and subtracted a sky composite acquired on the same night in that filter. After using the "disco-stu" routines developed by the Gemini staff to correct for distortion, we combined the dithers for each filter together with a median filter and corrected for zero-point offsets in the background by devising our own bad pixel masks for the data to eliminate residual edge effects and bad columns. The two pointings then combine into a single image by merging their data in the region of overlap. The resulting images have a plate scale of 0.″0195 per pixel, and cover a region 95″ in R.A. by 173″ in decl. The FWHM of the point-
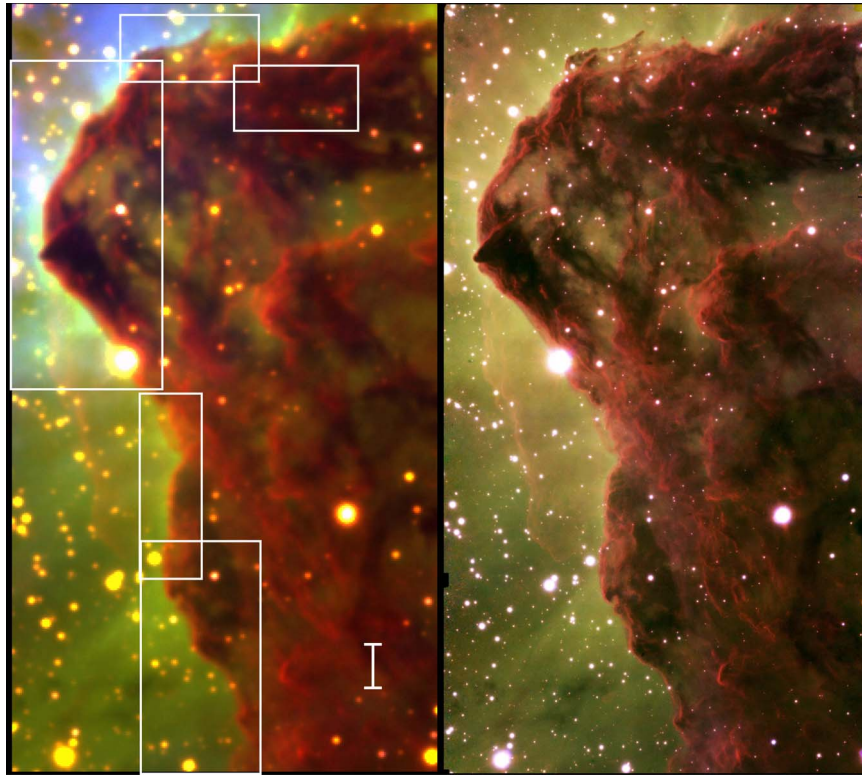
**Figure 2.** Images of Carina's Western Wall. Left: a non-AO image of the region from Hartigan et al. (2015) taken in $0.''8$ seeing, with $H_2$ in red, Br-$\gamma$ in green, and [O III] $\lambda 5007$ in blue. White boxes identify the regions expanded in Figure 3. The scale bar is 0.1 pc ($8.''97$). Right: the new AO images acquired with GSAOI, where $H_2$ is in red, Br-$\gamma$ in green, and K-continuum in blue. The FWHM of the stellar images ranges from $0.''065$ to $0.''11$.

(The data used to create this figure are available.)

spread function of the final images varies between $0.''065$ near the center of each of the pointings, to $0.''110$ near the edges, where stellar images become slightly distorted. These numbers compare well with the theoretical Rayleigh limit of $0.''069$ for the Gemini 8 m telescope at 2.2 $\mu$m. For comparison, JWST should achieve a resolution of $0.''085$ at this wavelength.

To improve the signal to noise we rebinned the AO images by $3 \times 3$ pixels, so the images we present here have square pixels of size $0.''0585$. There are 80 stars in the GAIA-DR2 catalog that have unsaturated profiles in our composite image, and the scatter in their positions was rather large, $\pm 0.''3$. Using the IRAF routines *geomap* and *geotran* we redid the distortion corrections and were able to reduce the scatter in the GAIA-DR2 stellar coordinates by a factor of 15, to $\pm 0.''02$ in each of the three filters. Figure 2 compares our final AO composite with a ground-based non-AO image of the same region.

### 3. Discussion

#### 3.1. Structure and Outflows within the Western Wall

The new AO images resolve previously unseen structure in the Western Wall on scales between the seeing limit of the ground-based images ($0.''8$; 1840 au) and the diffraction limit of Gemini at 2.2 $\mu$m ($0.''065$; 150 au). The composite image in Figure 2 illustrates that this size range is particularly rich in detail across the field of view, especially in $H_2$, which traces the photodissociation fronts. In the $H_2$ image, the apex area of the Western Wall appears as a series of long ridges that run along the interface, with projected spacings of $\sim$2000 au (Figure 3). A large triangular-shaped dark clump marked "Nose" protrudes

from the wall near the apex. The northern boundary of the Wall appears more chaotic than the apex does, and is home to a series of swept-back fragments of width $\sim$1800 au. To the south, the Wall exhibits a remarkable set of wave-like interfaces, including one that appears almost perfectly sinusoidal with a half-wavelength of 2500 au.

From the color composite image in Figure 2 one might easily get the impression that the Wall is transparent where $H_2$ emission is absent, because Br-$\gamma$ is present between the filamentary $H_2$ emission. However, in optical images the entire region where $H_2$ radiates is opaque, so it is likely that the Br-$\gamma$ located within the Wall comes from photoevaporation from its near-side in the direction of the observer. If this interpretation is correct, this Br-$\gamma$ emission lies superposed upon the $H_2$, and should be blueshifted relative to the Br-$\gamma$ emission to the east of the Wall by $\sim$10 km s$^{-1}$, the sound speed of the photoevaporative flow.

In addition to tracing fluorescence along irradiated interfaces, $H_2$ also emits in shock waves along bipolar flows from stellar jets. Our images reveal that an $H_2$ feature noted previously as a possible shocked object (Tapia et al. 2006), resolves into four nested bow shocks, labeled B, C, D, and E in Figure 3, and a short linear feature, denoted A, located upstream (east) of the bow shocks. These objects differ from the irradiated interfaces in that they have no associated Br-$\gamma$ or K-continuum emission (pure red color in Figure 2). The region also stands out from the other $H_2$ emission in the non-AO ground-based images (Tapia et al. 2006; Hartigan et al. 2015; left panel of Figure 2), but with much less clarity. The driving source of the jet is unknown. There is a narrow dark gap
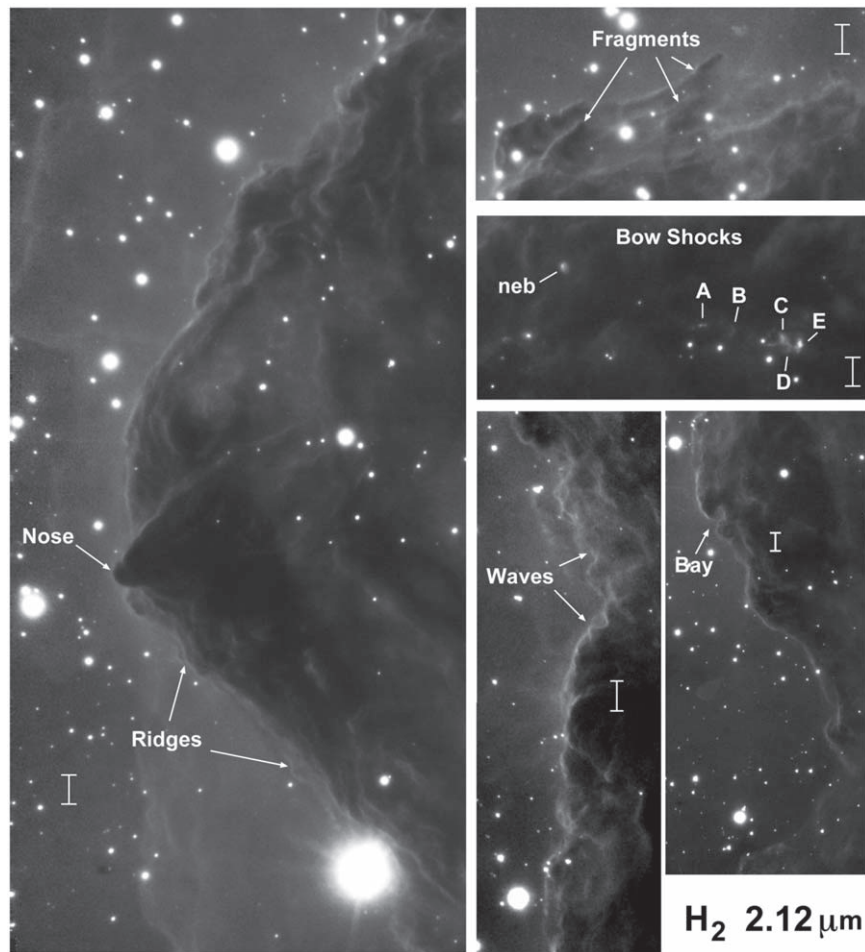
**Figure 3.** Expanded views of sections of the $H_2$ AO image of Carina's Western Wall. Scale bars are 5000 au ($2\farcs17$), assuming a distance of 2.3 kpc. Left: the apex of the Wall consists of 3–4 long parallel ridges and a large triangular-shaped protuberance labeled "Nose." Top right: the northern edge of the Wall reveals several swept-back fragments along the boundary of the object. Top middle: an outflow is defined by a series of $H_2$ bow shocks. Bottom right panels: the southern edge of the Wall has a complex, and at times sinusoidal-like, boundary and several overlapping arcs.

between knot A and a faint nebula $\sim0\farcs6$ to the east that could represent an opaque disk, and another possibility for a driving source is the star labeled "neb" in Figure 3 located $11\farcs5$ at PA $66\fdg5$ from knot A. This star has a conical-shaped reflection nebula aligned in the direction of the $H_2$ bow shocks, but no nebulae connect the star with the $H_2$ shocks. The Vela-Carina legacy survey with Spitzer did not detect any mid-infrared point sources at the position of knot A, though the nebulous star is visible faintly at 3.6, 4.5, and 5.8 $\mu$m. MHO 1630 is not obviously associated with a nearby filament of faint optical emission lines (Tapia et al. 2006), or with any sources visible in Spitzer or Herschel images (e.g. Tapia et al. 2015). Future ALMA mapping of the continuum and molecular line emission in the vicinity of MHO 1630 would clarify whether or not protostars exist there. Table 1 presents coordinates for several of the features shown in Figure 3.

**Table 1**
Coordinates for Objects in Figure 2

| Name | $\alpha$ (2000) | $\delta$ (2000) |
|---|---|---|
| neb | 10:43:29.548 | −59:34:10.695 |
| MHO-1630 A | 10:43:28.179 | −59:34:15.154 |
| MHO-1630 B | 10:43:27.860 | −59:34:15.570 |
| MHO-1630 C | 10:43:27.367 | −59:34:16.132 |
| MHO-1630 D | 10:43:27.294 | −59:34:16.805 |
| MHO-1630 E | 10:43:27.195 | −59:34:16.578 |
| Nose[a] | 10:43:35.813 | −59:34:48.752 |
| Wave[b,c] | 10:43:31.684 | −59:34:33.942 |
| Bay[c] | 10:43:31.772 | −59:36:02.958 |

**Notes.**
[a] Apex location.
[b] Southern of the two waves marked in Figure 3.
[c] Center of feature.

### 3.2. Theoretical Implications

The AO images in Figures 2 and 3 allow us to observe the irradiated interfaces in the Western Wall with unprecedented resolution, with implications for models of triggered star formation. In a simple one-dimensional model, we expect the D-front associated with an irradiated interface to increase the density in the cloud as the ionization front propagates, leading generally to conditions that are more favorable to gravitational collapse. In agreement with this general picture, ALMA observations along the southern portion of the Western Wall show that the densest portions of the molecular cloud lie along the dissociation front (P. Hartigan et al. 2020, in preparation). In three dimensions, compression behind a D-front becomes more complex. On a timescale of $\sim10^5$ yr, as a front passes

through clumps it will compress them, and shadowing leaves behind a pillar with a dense knot at the apex which might then collapse to form a new star (e.g., Figure 2 of Mackey & Lim 2010). Compression is highest when the front wraps around the clumps (Tremblin et al. 2012), and the external magnetic field can also influence the overall shape of the pillar (Henney et al. 2009).

If stars are indeed forming all along the Wall in response to the D-front, we would expect pillars to trail behind the newly formed stars away from the direction of radiation. However, in contrast to the pillar-rich southern region of the Carina Nebula (Smith et al. 2000), the AO images do not show any indication that the Western Wall breaks into pillars on size scales down to ∼150 au. Instead, we observe more of a smooth, slightly wavy, and sometimes ridged surface along much of the Wall down to the resolution of the images. The "Nose" in Figure 3 is the only feature where one can make a case that radiation may be wrapping around a clump. While this feature is striking and may form one or more pillars at some point, it is currently a rather broad structure, and it is unclear whether or not protostars or multiple cores exist there and, if so, whether those clumps predated the passage of the front. The available ALMA data on the Western Wall cover only its southern parts, and the Nose has not been observed yet. Future high-resolution millimeter observations might reveal the presence of protostars in this region.

The regularly spaced ridges that run parallel to the photodissociation front are a striking feature of the Western Wall. Their geometry implies a preferred direction for the ridges, characteristic of a dynamically significant large-scale magnetic field. Radiation-MHD simulations of H II regions show that there should be a large-scale magnetic field in the neutral gas that aligns along the direction of the D-front (Arthur et al. 2011). Comparing with the results of Mackey & Lim (2011), we see that their model R8 most closely resembles the ridges we see here. These simulations imply there should be a large-scale dynamically significant magnetic field oriented northeast to southwest in the Western Wall, parallel to the ridges. This prediction can be tested by measuring the dust polarization along the Wall.

The flocculent nature of the northern edge of the Wall differs markedly from the generally smoother, ridged morphology present near the apex. If the northern edge were strongly sculpted by the incident radiation from Tr 14, then the dense structures here should form pillars that point back toward the radiation sources to the east. Instead, the northern interface resembles one subject to Kelvin–Helmholtz (KH) instabilities (Frank et al. 1996; Jones & Downes 2012). If the orientation of the global magnetic field is approximately constant, and aligned as described above, then the field will be nearly perpendicular to the northern edge and thus will not tend to stabilize the system against the KH instability. The remaining ingredient for the KH instability is, of course, a shear flow. Radiation from nearby O-stars in Tr 14 and Tr 16 is capable of causing just such a shear flow along this edge and, indeed, the radiation itself may destabilize the system further (e.g., Shadmehri et al. 2012).

On a final note, it is particularly intriguing that the projected width of the ridges referred to above, the scale of the density structures along the northern edge of the Wall, and the wavelength of the sinusoidal structure referred to in Section 3.1 are all approximately 2000 au in size. This is well within the scales we would expect to be influenced by ambipolar diffusion in the undisturbed molecular cloud, and therefore below the length scales expected to be produced by turbulence (e.g., van Loo et al. 2008; Downes & O'Sullivan 2011; Downes 2012; Xu et al. 2019). Ambipolar diffusion is usually significant only in weakly ionized regions and it is therefore tempting to suppose that structures of this scale are created by flows at the surface of the molecular cloud, where the ionization fraction is high, rather than being "uncovered" as photoevaporation of the cloud proceeds.

## 4. Summary

The $H_2$, Br-$\gamma$, and K-continuum AO images Carina's Western Wall presented in this Letter reveal several unexpected structures within this classic irradiated molecular cloud that are difficult or impossible to discern from non-AO ground-based images. The Wall has a convex geometry so the interfaces appear as sharp tangent lines across the cloud, and are ideal for resolving interface shapes that provide clues to MHD instabilities. The apex of the Wall, which points in the general direction of the irradiating sources, consists of series of ridges that follow along the front. Wave-like structures also occur along the front. The most chaotic morphologies occur along the northern and southern edges of the Wall, where pillar-like fragments are present. These fragments do not point toward the irradiating sources, but are swept back as expected in a shear flow. The images also resolve the $H_2$ object MHO 1630 into an outflow that consists of a series of nested bow shocks without a clear driving source.

The observed ridging in the Wall argues for the presence of a large-scale dynamically important magnetic field, while the flocculent appearance along the northern and southern boundaries is a characteristic of KH instabilities. We find no direct evidence that the ionization front triggers new stars to form, in that there are no obvious cases where the front wraps around a dense clump to form a protostar. Nonetheless, the ionization front does encompass the entire Wall, and increases the density along the surface where radiation is absorbed.

These observations make it clear that size scales between ∼200 and 2000 au are rich with detail for an irradiated dark cloud, and in many ways hold the key to understanding the complex dynamical processes that sculpt these systems. The ridges, fragments, and waves we found all have sizes in this range, and require subarcsecond resolution to resolve even for the nearest regions of massive star formation. This capability now currently exists with AO imaging, but should expand greatly once JWST becomes operational. The interplay between large-scale, global physics such as magnetic field strengths and direction, rotation, and Jeans lengths, with the small-scale three-dimensional morphologies and complex motions induced by radiative feedback and turbulence continues to make star formation a challenging and engaging field of study.

Hartigan, Downes, & Isella

*Facility:* Gemini (GSAOI).

## ORCID iDs

Patrick Hartigan ⬤ https://orcid.org/0000-0002-5380-549X
Turlough Downes ⬤ https://orcid.org/0000-0002-7639-5446
Andrea Isella ⬤ https://orcid.org/0000-0001-8061-2207

## References

Arthur, S. J., Henney, W. J., Mellema, G., de Colle, F., & Vaźquez-Semadeni, E. 2011, MNRAS, 414, 1747
Bally, J., Ginsburg, A., Silva, D., & Youngblood, A. 2015, A&A, 579, A130
Carlsten, S. G., & Hartigan, P. 2018, ApJ, 869, 77
Cheng, Y., Tan, J. C., Liu, M., et al. 2018, ApJ, 853, 160
Downes, T. P. 2012, MNRAS, 425, 2277
Downes, T. P., & O'Sullivan, S. 2011, ApJ, 730, 12
Frank, A., Jones, T. W., Ryu, D., & Gaalaas, J. B. 1996, ApJ, 460, 777
Gagné, M., Fehon, G., Savoy, M. R., et al. 2011, ApJS, 194, 5
Goicoechea, J. R., Pety, J., Cuadrado, S., et al. 2016, Natur, 537, 207
Goicoechea, J. R., Santa-Maria, M. G., Bron, E., et al. 2019, A&A, 622, 91
Hartigan, P., Reiter, M., Smith, N., & Bally, J. 2015, AJ, 149, 101
Haworth, T. J., & Harries, T. J. 2011, MNRAS, 420, 562
Henney, W. J., Arthur, S. J., de Colle, F., & Mellema, G. 2009, MNRAS, 398, 157
Jones, A. C., & Downes, T. P. 2012, MNRAS, 420, 817
Krumholz, M. R., Klein, R. I., & McKee, C. F. 2011, ApJ, 740, 74
Li, P. S., Klein, R. I., & McKee, C. F. 2018, MNRAS, 473, 4220
Lim, B., Naze, Y., Gosset, E., & Rauw, G. 2019, MNRAS, 490, 440
Mackey, J., & Lim, A. J. 2010, MNRAS, 403, 714
Mackey, J., & Lim, A. J. 2011, MNRAS, 412, 2079
Pelligrini, E. W., Baldwin, J. A., Ferland, G. J., Shaw, G., & Heathcote, S. 2009, ApJ, 693, 285
Robitaille, J.-F., Scaife, A. M. M., Carretti, E., et al. 2018, A&A, 617, A101
Rosen, A. L., Krumholz, M. R., McKee, C. F., & Klein, R. I. 2016, MNRAS, 463, 2553
Shadmehri, M., Enayati, Z., & Khajavi, M. 2012, Ap&SS, 341, 369
Smith, N., Egan, M. P., Carey, S., et al. 2000, ApJL, 532, L145
Tan, J. C., Beltra n, M. T., Caselli, P., et al. 2014, in Protostars and Planets VI, ed. H. Beuther et al. (Tucson, AZ: Univ. of Arizona Press), 149
Tanaka, K. E. I., Tan, J. C., & Zhang, Y. 2017, ApJ, 835, 32
Tapia, M., Persi, P., Bohigas, J., Roth, M., & Gomez, M. 2006, MNRAS, 367, 513
Tapia, M., Roth, M., & Persi, P. 2015, MNRAS, 446, 4088
Tremblin, P., Audit, E., Minier, V., & Schneider, N. 2012, A&A, 538, 31
van Loo, S., Falle, S. A. E. G., Hartquist, T. W., & Barker, A. J. 2008, A&A, 484, 275
Venuti, L., Prisinzano, L., Sacco, G. G., et al. 2018, A&A, 609, 10
Winter, A. J., Clarke, C. J., Rosotti, G., et al. 2018, MNRAS, 478, 2700
Wu, R., Bron, E., Onaka, T., et al. 2018, A&A, 618, A53
Xu, S., Ji, S., & Lazarian, A. 2019, ApJ, 878, 157